MICROMECHANISMS OF BRITTLE FRACTURE IN 2¼Cr-1Mo WELD METAL

P. Bowen, M.B.D. Ellis, M. Strangwood and J.F. Knott

Studies have been performed on 2¼Cr-1Mo weld-metal in an as-deposited condition. Non-metallic inclusions, rich in titanium and silicon, are observed to control cleavage fracture. Macroscopic testpiece failure can be seen to result directly from the fracture of individual inclusions located in polygonal ferrite. The most important single factor is the size of the inclusion, but inclusions located in coarse polygonal ferrite are the most deleterious to toughness. The critical rôle of tensile stress is confirmed by observations of unique initiation sites close to known positions of peak tensile stress.

INTRODUCTION

Recent studies have shown the importance of inclusions in initiating cleavage fracture in carbon-manganese weld-metals (Tweed and Knott (1,2), McRobie and Knott (3)). This paper considers the cleavage fracture of submerged arc 2¼Cr-1Mo weld-metals in the as-deposited condition. The toughness is assessed by the use of the fracture toughness, K_{Ic} and the microscopic cleavage fracture stress, σ_F^*. The value of σ_F^* is measured as a function of temperature for two types of blunt-notch test pieces, with different notch geometries. The research combines a detailed metallographic characterisation of the weld-metal with careful fractographic observations to establish the micro-mechanism of cleavage fracture in 2¼Cr-1Mo weld-metals.

EXPERIMENTAL

All tests were performed on a 2¼Cr-1Mo submerged arc weld-metal of the composition shown in TABLE 1. The experimental welds were supplied by Marchwood Engineering Laboratories. Details of the welding procedure are given elsewhere (O'Brien and Wolstenholme (4)).

Department of Metallurgy and Materials Science,
University of Cambridge

Test pieces of the dimensions shown in fig. 1 were machined from three separate welds of dimensions 80 x 80 x 35 mm transverse to the welding direction. Two series of testpieces could be extracted through the thickness, and these were machined from near to the top of the weld and near to the bottom of the weld. In this way weld toughness could be evaluated as a function of depth position. If the direction of welding is taken as the longitudinal (L) direction, then all testpieces were notched in the transverse-short transverse (TST) orientation. The microstructure of the weld cross-section is shown in fig. 2. Testpieces were tested in the as-deposited condition.

Testpieces used to evaluate the fracture toughness, K_{IC}, were prefatigued in accordance with the procedures laid down in BS5447 (5). Fracture toughness (K_{IC}) tests were performed in four-point bend but otherwise to BS5447, over the temperature range -196 to +20°C using a Mand servo-hydraulic testing machine of 100 kN capacity. The test temperature was controlled to ±2°C. Standard Hounsfield number 12 tensile specimens were machined from the weld cross-section at mid-thickness positions, taking care to ensure that the entire gauge length was cut from weld-metal. These were tested over the temperature range -196 to +20°C using a screw-driver Mand testing machine of 50 kN capacity. Notched-bend testpieces of two designs were tested in the temperature range -196 to -120°C, in a manner similar to that employed for the K_{IC} testpieces. For the notch geometries shown in fig. 1(b) and fig. 1(c), finite element analyses have been developed to calculate not only the magnitude of the maximum stress intensification, σ_{11} max, but also its position ahead of the notch root (for notch root radius, ρ = 0.25 mm, notch included angle, $\phi = 45°$, see Griffiths and Owen (6), and for ρ = 1.00 mm, $\phi = 90°$, see Wall and Foreman (7)).

TABLE 1 - Composition of 2¼Cr-1Mo weld-metal (wt.%)

C	Mn	Ni	Cr	Mo	Si	Cu	Ti	Al
0.075	1.35	0.38	2.26	1.05	0.38	0.13	0.018	0.037
P	S	As	Sn	Nb	V	B		
0.030	0.018	0.038	0.030	0.04	0.04	<0.001		

To limit machining damage at the root of the notch in the blunt-notch testpieces, the final notch depth and profile was notch-ground in steps of 25 μm.

The microstructures of the welds were studied using optical microscopy, scanning electron microscopy (SEM) and thin-foil transmission electron microscopy (TEM). Particular attention was paid to the measurement of the size distribution of inclusions.

These were measured using both SEM and TEM. Scanning electron microscopy was used to evaluate the inclusion size distributions not only on polished optical sections (back-scattered mode), but also on fatigue and ductile fracture surfaces. These measurements were normalised by viewing a total area of approximately 0.02 mm^2 in each case.

Careful fractographic observations were made of cleavage fracture surfaces to identify any initiation sites. In studying local bursts of cleavage fracture, regions fatigued at high values of fatigue stress-intensity, ΔK, proved particularly useful. Inclusion chemistry was measured qualitatively by in-situ X-ray microanalysis.

RESULTS

Mechanical Testing

Values of 0.2% proof stress over the temperature range -196 to 20°C are shown in fig. 3. No significant variation in hardness was observed in the as-welded condition as a function of weld depth. The as-deposited microstructure was significantly harder (V_H=325) than the grain-refined microstructure (V_H=300). Note the high room temperature proof stress value of 740 MPa.

Fracture toughness (K_{IC}) values obtained for the as-welded condition over the temperature range -196 to 20°C are plotted in fig. 4. Catastrophic brittle fracture occurred even at room temperature. K_Q values are quoted above -120°C because specimen size restrictions (5) are violated at these higher temperatures. Nevertheless, only at room temperature was the load clip-gauge displacement trace not linear to failure. No significant variation in fracture toughness is observed as a function of position (depth) in the weld.

The values of the microscopic (local) cleavage fracture stress, σ_F^*, are plotted as a function of temperature in fig. 5. These values of σ_F^* have been calculated from the appropriate stress-intensification calibrations obtained by finite element methods (6,7) fig. 6. It is reassuring that these two independent analyses calculate similar stress intensifications for the same notch geometry, see fig. 6. It is assumed that fracture initiates at the position of σ_{11}(max) ahead of the notch root. The measured failure load defines the fraction of the general yield load at which fracture occurs. No variation in the value of σ_F^* is observed either as a function of position in the weld, or as a function of temperature (i.e. the value of σ_F^* is temperature independent and appears to be constant for a given notch geometry, fig. 5). The values of σ_F^* (1930 ± 70 MPa) obtained from the notch profile ρ=1.00 mm, ϕ=90° are significantly lower than those (2120±90 MPa) obtained from the notch profile, ρ =0.25 mm, ϕ=45°, see fig. 5.

Metallography and Fractography

The microstructure of the weld, fig. 2, is clearly composed of two distinct regions. Areas of as-deposited (columnar) regions in individual weld-beads are surrounded by bands of reheated (grain-refined) material produced by the deposition of subsequent weld-beads. These microstructures were studied by thin-foil transmission electron microscopy and optical microscopy. The as-deposited regions consisted of prior austenite grain boundaries decorated with a layer of allotriomorphic (polygonal) ferrite, constituting a volume fraction of approximately 15%, and some primary Widmanstatten sideplates (2-5%). The remaining volume fraction comprised acicular ferrite. No attempts were made to differentiate between ferrite plate content and the surrounding microphase regions. The reheated (grain-refined) regions showed a ferritic structure consisting of allotriomorphic ferrite with elongated grain-boundary carbides. The mean thickness of the carbides was observed to be 110 nm, and the coarsest carbides present were 160 nm in thickness. Only traces of Widmanstatten or acicular ferrite were observed and the microphase content was very low. The mean ferrite grain size observed in the reheated regions was approximately 5 μm, with most grains in the size range 3-10 μm and the largest ferrite grains were of the order of 30 μm. The mean prior austenite grain size was found to be approximately 40 μm.

The inclusion size distributions measured from thin-foil TEM micrographs is shown in fig. 7. The total area viewed was approximately 0.004 mm^2. This distribution may be compared with those obtained by SEM of optical sections, ductile and fatigue fracture surfaces, figs. 8-10. Only minor differences in the inclusion size distributions are seen using SEM if inclusions are sized either on optical sections, fig. 8, or on fracture surfaces produced by fatigue and ductile microvoid coalescence, figs. 9 and 10, respectively. Major differences are observed if the distribution of inclusions sized by TEM is compared with that sized by SEM, for example, compare figs. 7 and 8. TEM measures numerous inclusions below the limit of resolution of SEM. In addition, large inclusions $\gtrsim$ 1 μm are removed from the foil during specimen preparation (leaving holes in the foil).

In the fatigue pre-cracks in K_{IC} testpieces (particularly in those testpieces machined from the bottom of the weld) local, non-catastrophic bursts of cleavage fracture were often observed. Such local cleavage bursts could be clearly observed to be initiated by single inclusions on individual cleavage facets, see fig. 11 for example. The sizes of these cleavage facets indicate that they arise from areas of coarse polygonal ferrite. It was therefore possible on a small number of testpieces to size 75 individual inclusions that were seen to have initiated local cleavage fracture. This size distribution of potent inclusions can be superimposed on the general size distribution of inclusions as shown in fig. 10.

For the testpieces machined from the top part of the weld, the active zone in front of the notches (up to 3 mm for some test piece geometries and test temperatures)was observed at low magnifications to have sampled mostly as-deposited weld-metal microstructure. No clear cleavage initiation sites could be found on any of the fracture surfaces of the sharp-crack or blunt-notch (ρ=0.25 mm, ϕ=45^0) testpieces machined from this part of the weld.

For the testpieces machined from the bottom part of the weld, the active zone in front of the notches sampled mostly reheated weld-metal microstructure. No clear cleavage initiation sites could be found on the fracture surfaces of the sharp-crack testpieces, and it was difficult to find clear intitiation sites in the blunt-notch (ρ = 0.25 mm, ϕ = 45^o) testpieces. However, in the blunt-notch testpieces with ρ = 1.00 mm, ϕ = 90^o, single cleavage initiation sites could be found on all four testpieces. An example is shown in fig. 12. These local cleavage sites could be observed to be unequivocably centred on a single inclusion in two of these testpieces - fig. 12. An X-ray microanalysis spectrum of this inclusion is shown in fig. 13. It is a deoxidation product rich in titanium and silicon. Moreover, the positions of cleavage initiation sites seen to be close to the positions of σ_{11}(max) calculated from the appropriate finite-element analysis (7) - see Table 2.

TABLE 2 - Comparison of observed position of initiation site with calculated position of peak tensile stress σ_{11}(max)*

σ_{nom}/σ_o at fracture	Position of observed initiation site below notch (μm)	Position of σ_{11}(max) below notch (μm)	Distance below notch over which stresses ≥ 0.95 σ_{11}(max) are maintained (μm)
1.73	670	710	570-1100
2.03	730	1050	700-1450
2.36	680	Beyond limit of analysis	
2.44	800	Beyond limit of analysis	

*for testpiece geometry, ρ = 1.00 nm, ϕ = 90^o, after (7)

DISCUSSION

Fractographic observations in blunt-notch testpieces of single cleavage initiation sites at known positions of peak tensile stress - TABLE 2, demonstrate the critical rôle of tensile stress in causing cleavage fracture. Previously the controlling rôle of ten-

sile stress could only be deduced, e.g. from temperature independent values of σ_F^*, also observed in this present study, fig. 5. In addition, the results emphasise the importance of events on the microstructural scale in controlling the fracture of a macroscopic testpiece. Note that the catastrophic failure of a testpiece of cross-section 12.7 x 12.7 mm^2 results from the fracture of a single 2.4 μm inclusion (fig. 12) and the penetration of this microcrack into the ferrite matrix. The critical fracture event is envisaged to be the cracking of the inclusion and the dynamic penetration of the microcrack into the matrix. (A similar micromechanism has recently been suggested for carbide-initiated cleavage fracture in pressure-vessel steel plate, Bowen et al.(8).) It is also plausible that "microcracks" resulting from decohered inclusions would be active in promoting cleavage fracture.

Observations of local bursts of cleavage fracture seen during fatigue pre-cracking indicate that the size of the inclusion is important - fig. 10. Indeed, from fig. 10 it is possible to define a lower limit of 0.9 μm to the size of potent inclusions. Substantial improvements in toughness would be predicted if inclusion sizes could be reduced below this limiting value. Welding procedures cannot be sufficiently controlled to reduce all inclusion sizes to below 0.9 μm, but improvements in toughness have been obtained by using modified electrodes to eliminate the tail of the inclusion size distribution $\gtrsim$ 5 μm (Judson and McKeown (9)).

Observations of cleavage initiation sites following catastrophic testpiece failure are much more difficult to observe. Consider the cleavage initiation site shown in fig. 12(b). The site consists of a 2.4 μm diameter inclusion located in a 30 μm polygonal ferrite grain. It is likely that this represented the most potent inclusion sampled by the stress-distribution ahead of the blunt notch (ρ = 1.00 mm, $\phi = 90^o$). For this notch geometry cleavage initiation sites could be located easily and a mean value of σ_F^* = 1930 MPa is calculated. For testpieces of different notch geometry (ρ = 0.25 mm, $\phi = 45^o$) but similar grain-refined microstructural condition, cleavage initiation sites could not be clearly located in general and a mean value of σ_F^* = 2120 MPa is obtained. If the same micromechanism of failure operates in testpieces of both notch geometries, then the difficulties associated with observing cleavage initiation sites, and the higher σ_F^* values obtained for the notch with ρ = 0.25 mm, ϕ = 45 , can be attributed to a sampling argument. If stresses $\gtrsim$ 0.95 σ_F^* are considered, then at failure the notch with ρ = 1.00 mm, $\phi = 90^o$ samples approximately five times the area of the notch with ρ = 0.25 mm, $\phi = 45^o$. It is plausible, therefore, that failure ahead of the notch with ρ=0.25 mm does not occur from the most potent inclusions but from inclusions situated in smaller polygonal ferrite grains, for which indentification of initiation sites by tracing back river-lines is difficult.

It is important to note that inclusions can also be deduced to

control cleavage fracture for the reheated condition by comparing the value of σ_F^* with the value of σ_F^* obtained for a clean plate steel in which carbides were shown to be the primary microstructural feature that controlled σ_F^* (8). For the reheated condition where the coarsest thickness observed is 160 nm, a value of σ_F^* = 3200 MPa would be predicted. This is clearly much higher than the value of σ_F^* = 2120 MPa observed for the weld metal, which reflects fracture from inclusions.

In as-deposited weld-metal no cleavage initiation sites could be found. This is consistent with a sampling argument because the polygonal ferrite content is only 15% in the as-deposited weld-metal. However, the values of σ_F^* and K_{IC} obtained from the as-deposited and reheated microstructures are closely similar and therefore it may be inferred that the dominant factor is the size of the inclusions, which will be constant for these two microstructural conditions. (Nevertheless, further experiments have shown that by reaustenitising to 1100 ^{0}C, followed by oil-quenching, the value of σ_F^* can be increased to 2700 MPa. This heat-treatment which will not affect the inclusion size distribution produces a uniform mixed-martensite (80%)-lower bainite (20%) with coarsest carbides of 36 nm in thickness. No initiation sites could be found, but for an equivalent microstructural condition in clean plate steel, a value of σ_F^* = 3690 MPa was obtained (8) and from which the role of inclusions can again be deduced for the weld-metal because the value of σ_F^* is lower at 2700 MPa).

For the sharp-crack situation in K_{IC} testpieces, initiation sites would be expected to be difficult to find because the sampling volume will be further reduced compared with the blunt-notch situation. It is more important to note, however, that higher values of σ_{11}(max) are generated ahead of a sharp-pre-crack, and therefore it is likely in a K_{IC} test that failure will result from the most potent inclusion only occasionally.

Finally, starting with the information shown in fig. 10, there should be potential for developing a statistical approach to cleavage fracture based on actual, observed microstructural events.

CONCLUSIONS

1. Non-metallic inclusions, rich in titanium and silicon, control the cleavage fracture of 2¼Cr-1Mo weld-metals.

2. Macroscopic testpiece failure can be observed to result directly from the fracture of individual inclusions greater than 900 nm in diameter located in allotriomorphic (polygonal) ferrite.

3. The most important single factor is the size of the inclusion, but inclusions located in coarse polygonal ferrite appear to be the most deleterious to toughness.

4. The critical rôle of tensile stress in promoting cleavage fracture is confirmed by observations of unique initiation sites close to known positions of peak tensile stress.

ACKNOWLEDGEMENTS

Support for two of the authors (MS, MBDE) from CASE awards from ESAB (UK) and BP (Engineering Group) is gratefully acknowledged. During the course of this work one of the authors (PB) was supported by a Goldsmiths' Junior Research Fellowship at Churchill College, Cambridge. Thanks are also due to Professor D. Hull for provision of research facilities.

REFERENCES

(1) Tweed, J.H. and Knott, J.F., ECF4, Vol. 1, 1982, pp. 127-133, EMAS, U.K.

(2) Tweed, J.H. and Knott, J.F., Met. Sci., Vol. 17, 1983, pp. 45-54.

(3) McRobie, D.E. and Knott, J.F., Mat. Sci. and Tech., Vol. 1, 1985, pp. 357-365.

(4) O'Brien, T.J. and Wolstenholme, D.A., CEGB Research Report, TPRD/M/1356/R84.

(5) Plane Strain Fracture Toughness Testing of Metallic Materials, BS5447, 1977.

(6) Griffiths, J.R. and Owen, D.R.J., J. Mech. Phys. Sol., Vol. 19, 1971, pp. 419-431.

(7) Wall, M. and Foreman, A.J., Harwell Report, R11618, AERE UKAEA, (1985).

(8) Bowen, P., Druce, S.G. and Knott, J.F., in press Acta metallurgica, Lancaster, 1986.

(9) Judson, P. and McKeown, D., Weld. Inst. Autumn Conference, 1982, pp. 3.1-3.8.

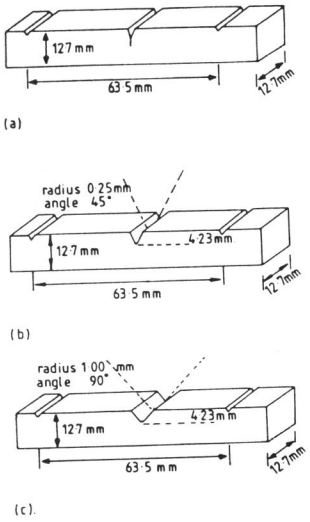

Fig. 1 Testpiece geometries

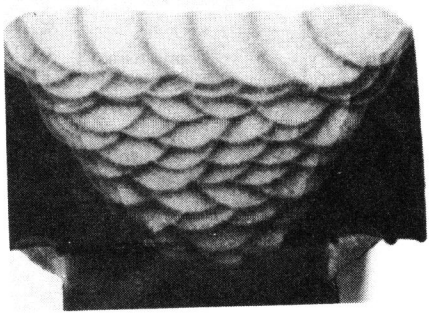

Fig. 2 Macrostructure of multi-pass weld

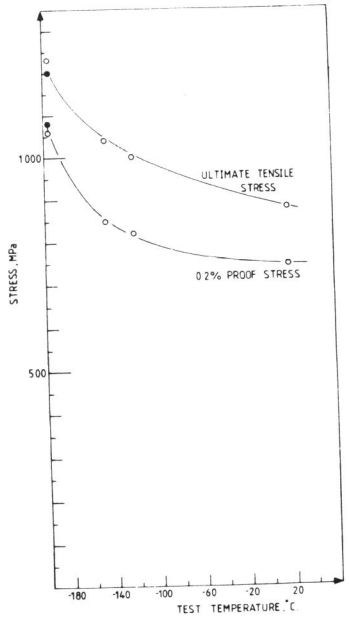

Fig. 3 Tensile properties

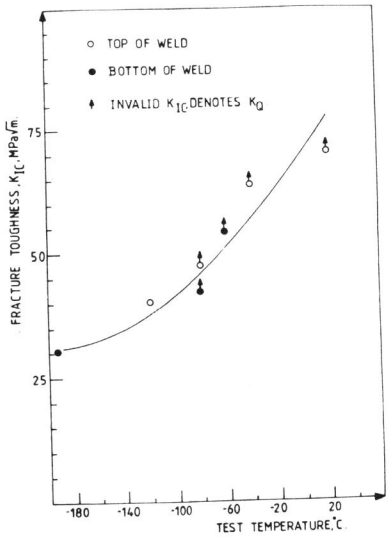

Fig. 4 Temperature dependence of the fracture toughness

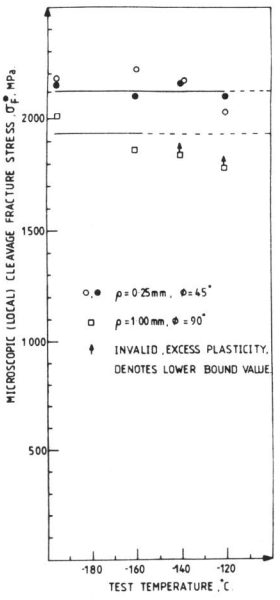

Fig. 5 Temperature dependence of the microscopic cleavage fracture stress

□ ρ=0.25 mm, $\phi=45^0$ } after Wall and Foreman (6)
Δ ρ=1.00 mm, $\phi=90^0$ }

o ρ=0.25 mm, $\phi=45^0$ } after Griffiths and Owen (5)

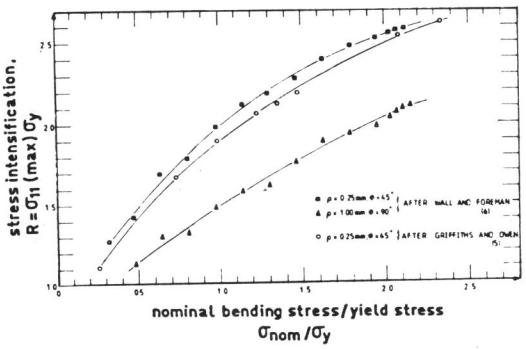

Fig. 6 Variation of stress-intensification with applied load

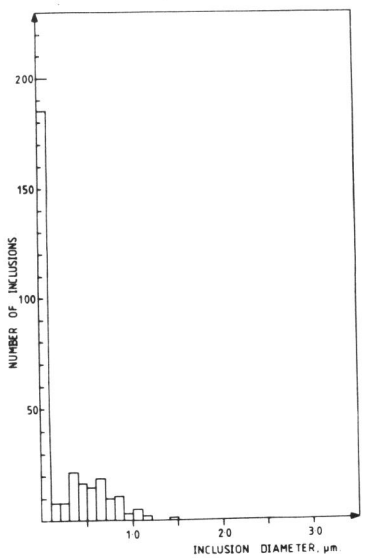

Fig. 7 Inclusion size distribution measured on thin-foils (TEM)

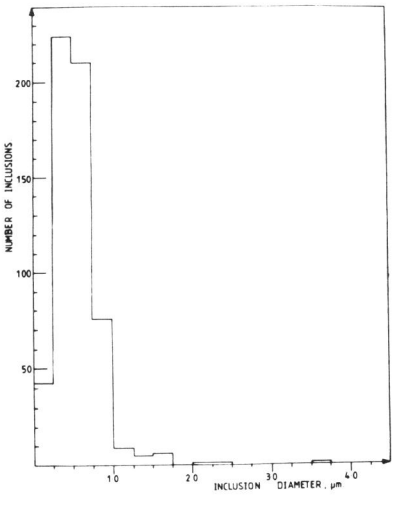

Fig. 8 Inclusion size distribution measured on optical sections (SEM)

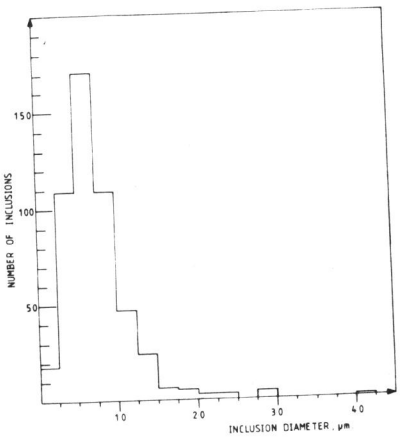

Fig. 9 Inclusion size distribution measured on areas of ductile fracture (SEM)

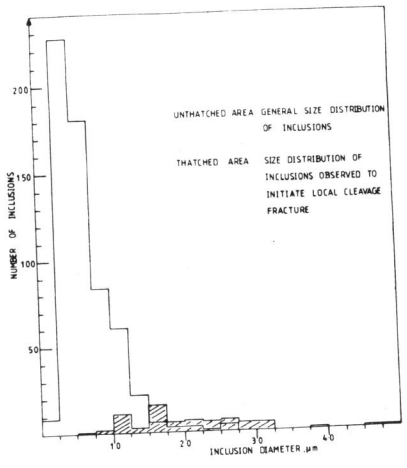

Fig. 10 Inclusion size distribution measured on areas of fatigue (SEM)

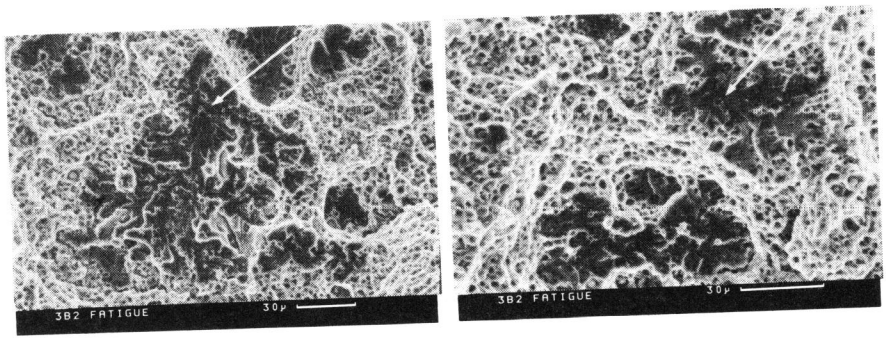

Fig. 11 Local cleavage fracture during fatigue loading

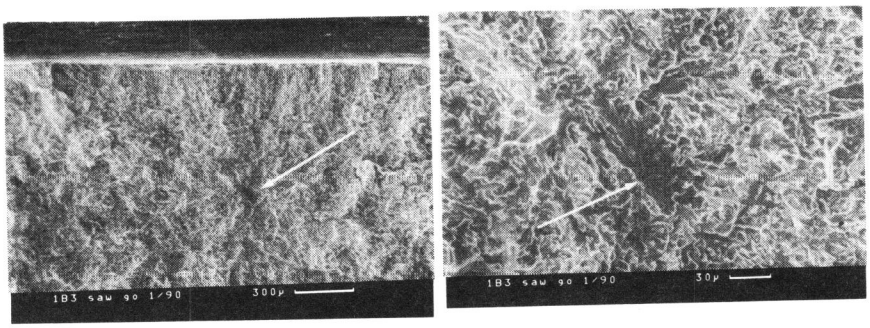

(a) (b)

Fig. 12 Cleavage initiation site

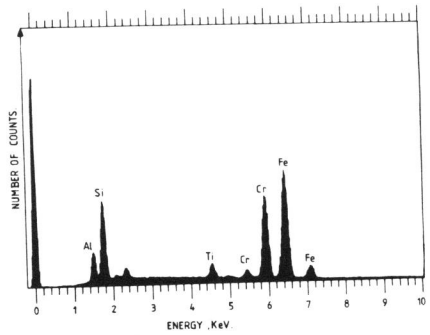

Fig. 13 Qualitative X-ray microanalysis of inclusion chemistry